

## Transmembrane Peptide NB of Influenza B: A Simulation, Structure, and Conductance Study<sup>†</sup>

W. B. Fischer,<sup>\*,‡</sup> M. Pitkeathly,<sup>§</sup> B. A. Wallace,<sup>||</sup> L. R. Forrest,<sup>‡</sup> G. R. Smith,<sup>‡</sup> and M. S. P. Sansom<sup>‡</sup>

Laboratory of Molecular Biophysics, Department of Biochemistry, University of Oxford, South Parks Road, Oxford OX1 3QU, U.K., Oxford Centre for Molecular Science, South Parks Road, Oxford OX1 3QT, U.K., and Department of Crystallography, Birkbeck College, University of London, Malet Street, London WC1E 7HX, U.K.

Received May 1, 2000

**ABSTRACT:** The putative transmembrane segment of the ion channel forming peptide NB from influenza B was synthesized by standard solid-phase peptide synthesis. Insertion into the planar lipid bilayer revealed ion channel activity with conductance levels of 20, 61, 107, and 142 pS in a 0.5 M KCl buffer solution. In addition, levels at  $-100$  mV show conductances of 251 and 413 pS. A linear current–voltage relation reveals a voltage-independent channel formation. In methanol and in vesicles the peptide appears to adopt an  $\alpha$ -helical-like structure. Computational models of  $\alpha$ -helix bundles using  $N = 4, 5,$  and  $6$  NB peptides per bundle revealed water-filled pores after 1 ns of MD simulation in a solvated lipid bilayer. Calculated conductance values [using HOLE (Smart et al. (1997) *Biophys. J.* 72, 1109–1126)] of ca. 20, 60, and 90 pS, respectively, suggested that the multiple conductance levels seen experimentally must correspond to different degrees of oligomerization of the peptide to form channels.

In the genome of influenza B, RNA segment 6 encodes two integral membrane proteins, NB and NA. NB is a protein of ca. 100 amino acids. It has ca. 18 extramembraneous residues on its N-terminal end, a 22-residue membrane spanning segment, and a ca. 60 residue long C-terminal end (1, 2). NB is expressed at the surface of infected cells (3–5). In the virion the N-terminal site is located at the external surface. Experiments with gold immunolabeled freeze-fractured virions indicate that the C-terminus is located at the inside of the virion (4). By analogy with the M2 protein of influenza A, it was suggested (reviewed in ref 6) that NB might be a channel-forming protein.

Conductance measurements with purified NB expressed in *Escherichia coli* and reconstituted in lipid bilayers reveal a conductance of 45 pS. However, when NB is incorporated in liposomes and then added to planar lipid bilayers, the conductance ranged from ca. 10 pS at very low NB concentration in the liposomes to several hundred picosiemens for higher concentrations (7). At neutral pH the channels are more permeable for sodium ions than chloride ions ( $P_{\text{Na}}/P_{\text{Cl}} \approx 9$  at pH 6.5). In asymmetrical NaCl solutions at pH 2.5 the permeability is higher for chloride ions ( $P_{\text{Cl}}/P_{\text{Na}} \approx 4$ ). A recent study on NB expressed in the plasmalemma of MEL<sup>1</sup> cells showed that the channel peptides induce a  $\text{Na}^+$ -dependent proton current and a pH-activated  $\text{Cl}^-$  current (8).

One way in which single integral membrane proteins can form ion channels is via oligomerization to form a bundle

of transmembrane helices. For the analogous channel peptide in influenza A, M2, it is believed that a tetrameric  $\alpha$ -helix bundle is the minimal form of the proton-permeable ion channel (9–11). For NB the number of subunits in the bundle is not known. Purification of NB on gels using nonreducing conditions revealed the formation of disulfide-linked dimers and higher oligomers (2). Molecular modeling studies on bundles of the transmembrane parts of the peptide have been performed in vacuo with four, five, and six segments (12). Comparison of experimental conductance data (7) with conductance calculations using HOLE (13, 14) suggests that pores from NB might contain five helices. It was suggested that Ser-20, Thr-24, and Ser-28 face the pore and generate partially a hydrophilic wall within the channel. The hydroxy groups could guide the  $\text{Na}^+$  or the  $\text{Cl}^-$  ions via either the oxygens or their protons.

In a previous computational study (15) we showed that 28 residues is an optimal length for synthetic transmembrane-spanning peptides of the viral ion channel peptides. Therefore, in this study computational and experimental studies are undertaken with the NB 28mer consisting of the sequence IRGS<sup>20</sup>IIITICVSLI<sup>30</sup>VILIVFGYIA<sup>40</sup>KIFI (NB, Lee).

### EXPERIMENTAL PROCEDURES

**Peptide Synthesis.** The transmembrane segment of NB (IRGS<sup>20</sup>IIITICVSLI<sup>30</sup>VILIVFGYIA<sup>40</sup>KIFI; NB, Lee) was synthesized using standard Fmoc methodology on an Applied

<sup>†</sup> This work was supported by the EC with a TMR fellowship to W.B.F. L.R.F. is a MRC student. M.S.P.S. is supported by the Wellcome Trust.

\* To whom correspondence and reprint requests should be addressed. E-mail: wolfgang@bioch.ox.ac.uk. Telephone: +44-1865-275776. Fax: +44-1865-275234.

<sup>‡</sup> University of Oxford.

<sup>§</sup> Oxford Centre for Molecular Science.

<sup>||</sup> University of London.

<sup>1</sup> Abbreviations: BES, *N,N*-bis(2-hydroxyethyl)-2-aminoethanesulfonic acid; CD, circular dichroism; Da, Dalton; DSSP, dictionary of protein secondary structure; MALDI-TOF, matrix-assisted desorption–ionization–time of flight; MEL, mouse erythroleukemia; MD, molecular modeling; NRMSD, normalized root mean standard deviation; POPC, 1-palmitoyl-2-oleoyl-*sn*-glycero-3-phosphatidylcholine; PVDF, poly(vinylidene difluoride); SUV, small unilamellar vesicles; SPC, single point charge; TFA, trifluoroacetic acid; TM, transmembrane; RMSD, root mean square deviation.

Biosystems 430A automated peptide synthesizer. PAC-PEG-PS resin and HATU coupling reagent purchased from PE Biosystems were used. Each synthesis cycle incorporated double coupling of the residues using a 10-fold excess of the amino acid. Temporary  $\alpha$ -N Fmoc-protecting groups were removed by 20% piperidine in DMF after a capping step involving incubation with 0.5 M pyridine and 0.5 M acetic anhydride. The peptide was purified by preparative HPLC using a POROS RP 4.6  $\times$  100 mm column at a flow rate of 5 mL/min. The buffers used were A = water [0.1% TFA (trifluoroacetic acid)] and B = acetonitrile (0.1% TFA). A gradient was run between 5% and 50% B over 20 min. Matrix-assisted laser desorption-ionization-time of flight spectrometry (MALDI-TOF) was done on a Micromass TofSpec 2E mass spectrometer operating in the linear mode from an  $\alpha$ -cyano-4-hydroxycinnamic acid matrix. The sample concentration was 3 pmol/ $\mu$ L using external calibration. A single peak with an average mass of 3092.88 Da (MH<sup>+</sup>) was found [calculated average 3092.96 Da (MH<sup>+</sup>)]. For automated amino acid sequence determination samples were adsorbed onto PVDF membrane [poly(vinylidene difluoride), 0.2  $\mu$ m porosity] using a ProSorb cartridge (PE Biosystems, Warrington, U.K.) and following the manufacturer's protocol. The membrane-bound samples were then excised from the ProSorb cartridge and N-terminally sequenced on an Applied Biosystems 494A "Procise" sequencer (PE Biosystems, Warrington, U.K.).

**Circular Dichroism (CD) Spectroscopy.** CD spectra were recorded on a AVIV 62ds spectropolarimeter equipped with a variable position detector for use with scattering (membrane) samples. Spectra reported have been obtained with the maximum acceptance angle  $\geq 90^\circ$  (16). The wavelength range scanned was 300–185 nm with a step width of 0.2 nm. Either 0.01 cm (protein in methanol) or 0.05 cm (vesicle suspensions) path-length optical cells were used. Samples in methanol were recorded at 10 °C and vesicle suspensions at 20 °C. Each sample spectrum represents an average of five scans for each of three independently prepared samples.

Methanol (spectrophotometric grade, Aldrich) solutions contained 2 mg/mL peptide. For vesicle suspensions, 0.7 mg of protein was added to 8.7 mg of 1-palmitoyl-2-oleoyl-*sn*-glycero-3-phosphatidylcholine (POPC) to obtain a lipid:protein ratio of 50:1 (w/w). After being dissolved in 300  $\mu$ L of methanol/100  $\mu$ L of CHCl<sub>3</sub>, the solvent was removed in a rotary evaporator under vacuum, leaving a thin film on the round-bottom flask. This film was hydrated with 1 mL of deionized H<sub>2</sub>O and sonicated in a cylindrical ultrasonic bath (Laboratory Supplies) for ca. 10 min at ca. 30 °C. Further sonication was undertaken with a probe sonicator (Soniprep 150), applying 5 s bursts in intervals of 30 s in a water-jacketed cell at room temperature. After centrifugation for ca. 2 min at 12800g, the supernatant, which contained small unilamellar vesicles, was used for the measurements. The final lipid-to-protein ratio was determined using ca. 300 mL of the vesicle suspensions for phosphate analysis.

The secondary structure of the protein was analyzed using a linear least-squares curve-fitting procedure (16). The reference data set was derived from 15 water-soluble proteins (17). The results were normalized to 100%, dividing each fraction by the sum of the fraction. The quality of the fit of the calculated structure to the data was determined by the normalized root mean standard deviation (NRMSD) (16)

parameter. In general, only NRMSD values of  $<0.1$  indicate strong correspondence between the experimental spectrum and the calculated secondary structure, although values of  $<0.2$  tend to indicate a general similarity of the type of calculated structure to the actual structure.

**Channel Recordings in Planar Lipid Bilayers.** Planar lipid bilayer was formed across an elliptical aperture (ca. 130  $\mu$ m diameter on the long axis) in a thin (25  $\mu$ m) Teflon film (Yellow Springs Instruments) (18). Approximately 40  $\mu$ L of lipid [10:1 (w/w) L- $\alpha$ -phosphatidylcholine (type II-s) and cholesterol, both from Sigma] in CHCl<sub>3</sub> was spread on top of a buffer (0.5 M KCl, 10 mM BES, pH 7.0) which was raised across the aperture. This resulted in ca. 0.2 mg of lipid on each side. After addition of the protein (dissolved in methanol) on the cis side (amplifier), the bilayer was formed by raising the buffer level. Electrical currents were recorded with an Axopatch 1D amplifier at a rate of 5 kHz and filtered with 1 kHz using a Digi Data 1200 interface (Axon Instruments). Currents were generated using a Function Generator TG 302, LEVELL, Barnet, U.K.

**Modeling and Simulations.** Models of bundles have been generated by in vacuo restrained molecular dynamics (MD) in a simulated annealing (SA) protocol as described previously (19), X-PLOR V3.1 (20) with the CHARMm PARAM19 parameter set (21). This gave us an ensemble of 25 models of a bundle. Models containing four, five, and six helices per bundle were generated. There was no preference for the bundles to form either a left-handed or right-handed supercoil, and so subsequent simulations were based on bundles with the most symmetric untilted structures for each ensemble. Each helix bundle thus generated was docked in holes of various radii in a preequilibrated lipid bilayer [of 1-palmitoyl-2-oleoyl-*sn*-glycero-3-phosphatidylcholine (POPC)] of area ca. 6  $\times$  6 nm<sup>2</sup> as described in detail elsewhere (22, 23). Each lipid/protein system was then solvated with more than 30 SPC water molecules per lipid. MD simulations were performed using GROMACS 1.6 (<http://rugmd0.chem.rug.nl/~gmx/gmx.html>). All simulations were of 1 ns duration. Simulations were run on either a 10 or an 80 SGI Origin 2000 processor. For a system of ca. 20 000 atoms the CPU time is ca. 8 days per nanosecond per processor. Subsequent analysis of the simulations used Gromacs and DSSP (24). Structures were visualized using Quanta (MSI) and Rasmol. Using the program HOLE (14) a pore radius profile was calculated, and the conductance was estimated.

## RESULTS

**Sequence.** The sequence used in the present study was IRGS<sup>20</sup>IIITICVSLI<sup>30</sup>VILIVFGYIA<sup>40</sup>KIFI (Figure 1). The only deviation from the natural sequence of the virus B/Lee/40 is a substitution of Cys-38 by Tyr (position 22 in the helical wheel). We justify this mutation by the fact that all other protein sequences known from NB show this substitution in this particular region.

**Secondary Structure.** In an attempt to experimentally ascertain the secondary structure of NB, circular dichroism (CD) spectroscopy was used to examine the peptide in methanol and in small unilamellar vesicles (SUVs) comprised of POPC (Figure 2). SUVs with high lipid-to-protein ratios were used for these studies because they have been shown

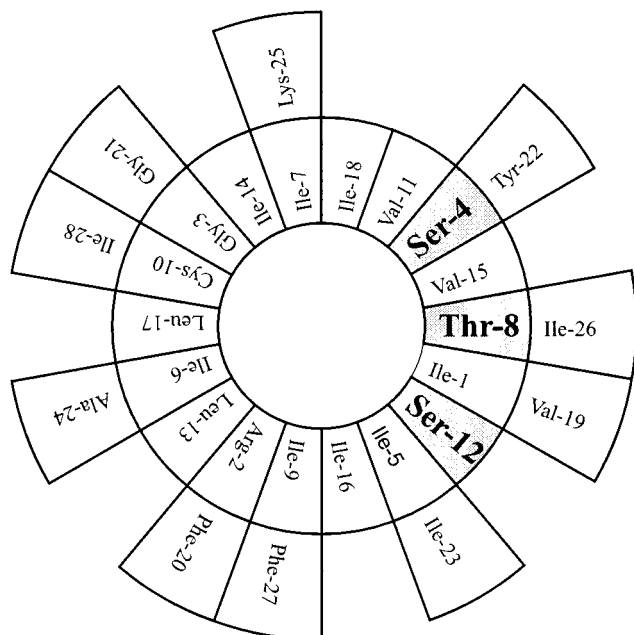


FIGURE 1: Helical wheel projection of the sequence of the putative transmembrane segment of NB.

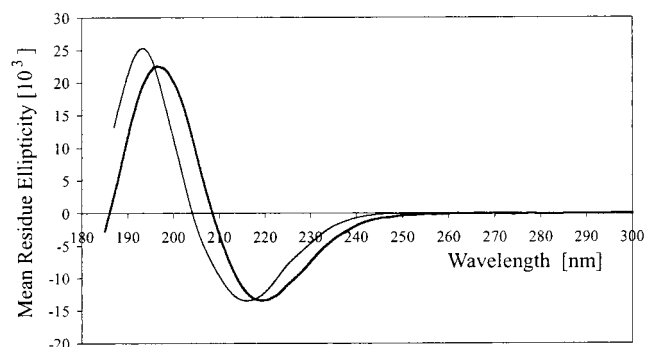


FIGURE 2: CD spectra of NB peptide in methanol (thin line) and in POPC vesicles (thick line).

to not produce significant differential scattering and absorption flattening artifacts that can be found with other membrane samples (25). The methanol spectrum exhibits peaks at  $\sim 193$  and  $217$  nm and a shoulder at  $\sim 224$  nm, with the magnitude ratio of the positive and negative peaks being approximately 2:1. Its appearance is neither that of a classical helix nor that of a classical sheet spectrum. Both the methanol and SUV spectra have similar waveforms, but the peaks in the vesicle spectrum are red shifted by  $\sim 3$  nm from those in the methanol spectrum. Secondary structure analysis of the methanol spectrum indicated a content of  $\sim 50\%$  helix, but with a high NRMSD parameter (0.14). The helical content of the vesicle sample was calculated to be 65%. However, its very high NRMSD (0.37) suggests a particularly poor fit to the reference database. Shifting the vesicle spectrum to a lower wavelength by 3 nm resulted in a better fit (NRMSD = 0.19), although the helix content essentially did not change (67%). Because of the poor fit (high NRMSD), the secondary structure determination based on this CD data is not very reliable but can only suggest the general sort of structure present. The high NRMSD is a strong indication that the peptide has spectral characteristics not represented in the reference database of soluble proteins. This circumstance could arise for two reasons: (1) The

environment of the lipid bilayer (and the nonaqueous solvent methanol) produces spectral characteristics unlike those in aqueous solution. This possibility has been explored in other peptide systems, and the blue shift observed in this case has been well characterized as a function of dielectric constant (26). This will result in a poor fit of the soluble protein reference database to the experimental data. Furthermore, because the  $n \rightarrow \pi^*$  and  $\pi \rightarrow \pi^*$  peaks shift to different extents, the shape of the curve will change, and the two negative peaks typical of an  $\alpha$ -helix tend to merge (27), leading to an overestimate of  $\beta$ -sheet. (2) The conformation of the peptide adopts may be considerably different than that found in regular secondary structural elements in proteins; in particular, the flexibility of the peptide may lead to "irregular helical structures" as suggested by the simulations, which have  $\Phi/\Psi$  angles that differ from typical helices [as has been previously observed for a small peptide (28)]. The irregular structure could either come under the category of "other" in the analyses or simply lead to a poor fit. It appears likely that both of these effects are manifest in the case of NB peptide. The magnitudes and ratios of the NB peaks located near 195 and 220 nm are larger than would be expected for  $\beta$ -sheets and smaller than would be expected for pure helices. Furthermore, the characteristic double negative peaks normally found for an  $\alpha$ -helix are only suggested by the shoulder at 224 nm. These are very different spectra than obtained for  $\alpha$ -helical peptide fragments from the influenza hemagglutinin protein (29, 30), again suggesting that the NB peptide is not a classical  $\alpha$ -helix structure.

To further explore the nature of its secondary structure, alternative calculation algorithms were tested with the data. They resulted in either negative fractions for the calculated secondary structures (31) or poor fits between the calculated and experimental spectra (32) or failure of one aspect of the algorithm to find a solution (33). The latter two methods produced results which indicated that both helical and sheet structures were present, but with the amount of helix greater than the amount of sheet. In both cases a significant amount of secondary structure was found to be "other".

In summary, the CD data indicate that similar secondary structures are present in vesicles and in methanol solution for NB and that while the secondary structures are not standard helices, helices are likely a significant component in each environment. This has led to the initial modeling of this peptide as helical for the simulation studies. However, it should be noted that, given the unusual nature of the spectra, they do not exclude completely an alternative structure, for example, such as some form of distorted  $\beta$ -sheet raft.

*Conductance in the Planar Bilayer.* In a typical bilayer experiment channel activity was observed with a peptide concentration of ca.  $3.2 \mu\text{M}$  (Figure 3A). Such channel activity could be repeated in two further experiments recorded at different days each with newly prepared peptide samples. Channel activity seems also to be sensitive to amantadine (Fischer and Sansom, unpublished results). The data sequence in Figure 3A represents an evolution in time, starting with the recordings at  $-100$  mV. After the transbilayer potential was applied, an increase in current was found. For the rest of the recordings the closed state (C) and this first conductance level (O1) have been hardly observed anymore. In all four major conductance levels O1–O4 were

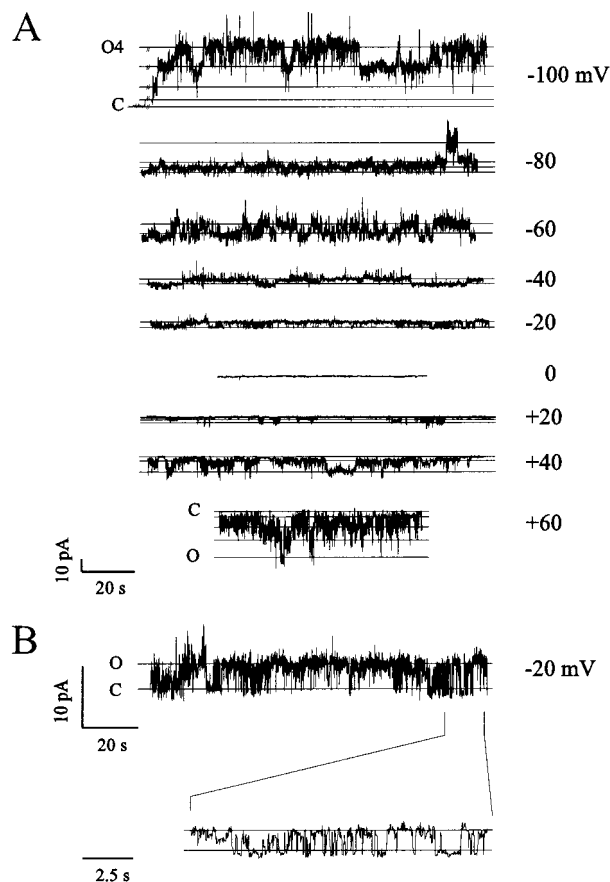


FIGURE 3: (A) Current activity of NB peptide incorporated in a planar lipid bilayer. NB was added to ca.  $3.2 \mu\text{M}$  to the cis side of a  $0.5 \text{ M}$  KCl solution buffered to pH 7 (BES). The buffer was equal on both sides of the chambers. (B) Current activity at  $-20 \text{ mV}$  applied external voltage. The trace is an expanded view from panel A. Data were filtered, resulting in a cutoff frequency of  $50 \text{ Hz}$ .

detected at  $-100 \text{ mV}$  with  $50$ ,  $130$ ,  $320$ , and  $470 \text{ pS}$ . The current amplitude histogram for the recording at  $-100 \text{ mV}$  is shown in Figure 4A. Most of the time the peptides are in the highest conductance states (O3 and O4) at  $-100 \text{ mV}$  membrane potential. A further increase in conductance level was not observed. At lower transmembrane potential ( $-80 \text{ mV}$ ) the highest conductance state is only rarely seen in the recordings. At  $-80$ ,  $-40$ , and  $-20 \text{ mV}$  the peptide primarily flickers between two conductance levels:  $104$  and  $62 \text{ pS}$  ( $-80 \text{ mV}$ ),  $134$  and  $60 \text{ pS}$  ( $-40 \text{ mV}$ ), and  $215$  and  $41 \text{ pS}$  ( $20 \text{ mV}$ ). At the transmembrane potential of  $+20 \text{ mV}$  the peptides form mostly channels with  $19$ ,  $52$ , and  $112 \text{ pS}$  and occasionally  $238 \text{ pS}$ . With increasing positive transmembrane potential ( $> +20 \text{ mV}$ ) the conductance levels become less resolved. The experimental conductance levels are listed in Table 1. Levels of  $20$ ,  $61$ , and  $107 \text{ pS}$  from experiments perfectly merge with the computational values. The higher conductance levels ( $251$  and  $413 \text{ pS}$ ) might be the consequence of assemblies greater than six segments with undefined topology and multiple channel openings due to the peptide concentration (7).

Analysis of the histograms of each trace in Figure 2A reveals distinct conductance levels which can be grouped to give average values for an individual level (Table 1). Figure 4B shows the current–voltage relationship of the currents which might belong to a single conductance level. The linear relation indicates an ohmic behavior of the pores and a

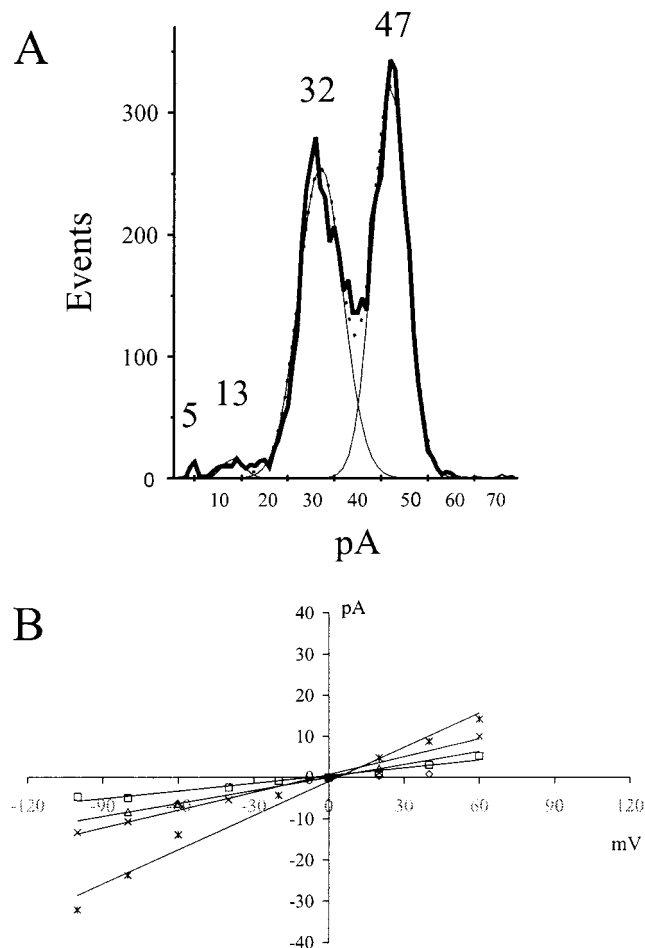


FIGURE 4: (A) Current histogram of the trace in Figure 3A recorded at  $-100 \text{ mV}$  transmembrane potential. The histogram is fitted with Gaussian-shaped bands. The data are corrected for the closed state shown in Figure 3A at the left side of the trace at  $-100 \text{ mV}$ . Lines: thin, fitted Gaussian curves; dotted, sum over all Gaussian curves. (B) I–V relationship of the currents found in Figure 3. Trend lines represent  $20 \text{ pS}$  (diamonds),  $61 \text{ pS}$  (squares),  $107 \text{ pS}$  (triangles),  $142 \text{ pS}$  (crosses), and  $251 \text{ pS}$  (stars).

Table 1: Estimated Conductance (in pS) for Solutions of KCl and NaCl<sup>a</sup>

	bundle 4	bundle 5	bundle 6
0.5 M KCl	22	56	88
(0.083 $\Omega \text{ m}$ calcd)			
0.5 M NaCl	13	34	53
(0.214 $\Omega \text{ m}$ calcd)			
0.5 M KCl (exptl)	$20 \pm 1.5$ , $61 \pm 17$ , $107 \pm 4$ , $142 \pm 17$ $251 \pm 41/413 \pm 81$		
no. of water molecules	49	105	145
minimal pore diameter (Figure 9A) (nm)	0.11	0.28	0.39

<sup>a</sup> Computational estimations are based on the hole diameter using HOLE and a subsequent conductance calculation. Conductance represents the average of five structures taken from the last 250 ps in steps of  $50 \text{ ps}$ . The number of water molecules is taken from the bundles after  $1 \text{ ns}$  (Figure 7).

voltage-independent channel formation. The histogram of the trace at  $-100 \text{ mV}$  is displayed in Figure 4A, corrected for the closed level.

The channel peptide shows different kinetics. The upper conductance level in Figure 3A has open times of  $20$ – $60 \text{ s}$ . The recording at  $-20 \text{ mV}$  shows open times in the millisecond range. An example of the recording on an expanded time scale is shown in Figure 3B. Frequent short jumps

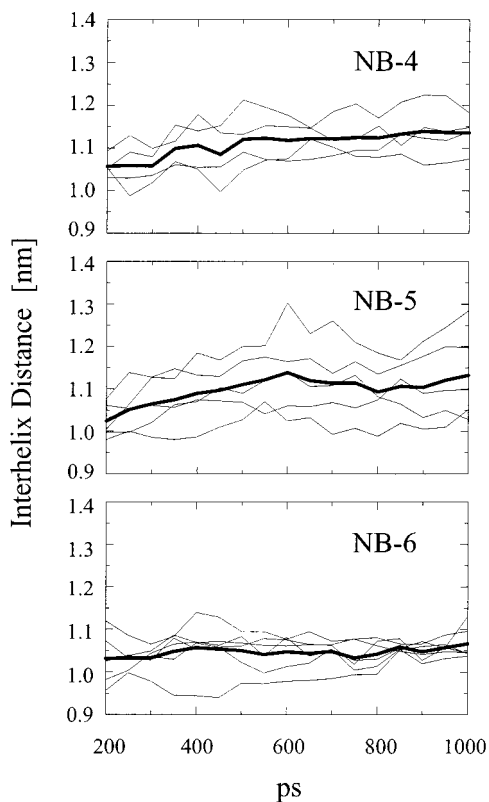


FIGURE 5: Interhelix distance between the individual segments in each bundle for NB-4 (top), NB-5 (middle), and NB-6 (bottom). Values are averaged over all segments and drawn with thick lines in each panel.

between conductance states have been reported previously and related to fast conformational changes of the segments (34).

**Computational Model of the Bundles.** Models of bundles were generated in such a way that the hydrophilic residues, serines and threonines, face the pore (Figure 1). Similar positions with respect to Ser and Thr have been used in simulations on M2 from influenza A (22, 35), the pore-lining segments of M2 from nicotinic acetylcholine receptor (nAChR) (36, 37), and a synthetic ion channel peptide Ac-(LSLLSL)<sub>3</sub>-CONH<sub>2</sub> (38). In the case of the nAChR the positions are experimentally confirmed (reviewed in refs 39–41). The placement of the Ser and Thr in the NB transmembrane segment consequently places the phenylalanines on the outside of each bundle. Such a location for tryptophans is found in other channels, e.g., porins (42). Lysines and arginines are located at the helix–lipid interface. Thus, the starting structure coincides with the current ideas of channel formation.

After a rise within the first 200 ps the RMSD values reach a plateau at ca. 0.17 and 0.25 nm for the rest of the simulation. These values are usually found for simulations of single-stranded peptides (15, 22) or bundles in a bilayer (43). The stability of the bundles is also represented by constant values for the interhelix distance of 1.0–1.1 nm in the second half of the simulation for all bundles (Figure 5).

Some of the single TM segments deviate from an ideal helical structure. A detailed analysis of the average  $\Phi$  and  $\Psi$  values reveals deviation from a pure  $\alpha$ -helix structure for NB-4 in one segment especially around Val-27 ( $\Phi = -66.9^\circ \pm 9.8^\circ$ ,  $\Psi = -28.1^\circ \pm 12.7^\circ$ ) and Ser-28 ( $\Phi = -88.9^\circ \pm$

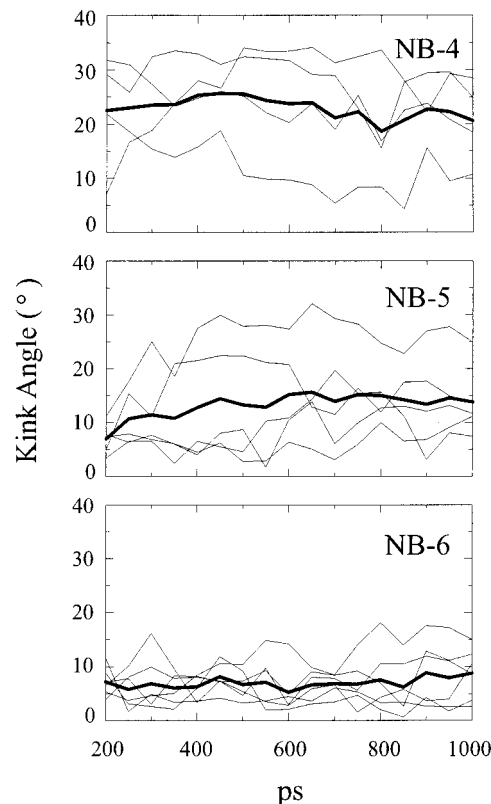


FIGURE 6: Helix kink angle (deg) from all segments of NB-4 (top), NB-5 (middle), and NB-6 (bottom). The averaged kink values are drawn in thick lines in each panel.

$15.5^\circ$ ,  $\Psi = -41.8^\circ \pm 10.9^\circ$ ). These residues are located almost in the middle of the segment. For another segment nearly all the residues show deviation from the normal  $\alpha$ -values ( $\Phi = -60^\circ$ ,  $\Psi = -50^\circ$ ) (44). The latter deviation is visualized by the bend of one of the segments (data not shown). Also, for NB-5 one segment shows strong deviation for some residues from the normal  $\Phi$  and  $\Psi$  values: Arg-18 ( $\Phi = -120.3^\circ \pm 12.0^\circ$ ,  $\Psi = -61.7^\circ \pm 31.5^\circ$ ) and Gly-19 ( $\Phi = -106.5^\circ \pm 33.0^\circ$ ,  $\Psi = -52.2^\circ \pm 15.7^\circ$ ). These deviations lead to a bent close to the N-terminal part of the segment. For NB-6 no major deviations are found. All segments in the bundle share a common feature that is a deviation from helicity at the ends of each helix (data not shown). As a result, there are different residues in each of the bundles causing the disruption of the ideal helix structure.

Throughout the simulation the average tilt of the bundles is not changed (data not shown). Tilt angles of  $4.8^\circ$  (NB-4),  $9.2^\circ$  (NB-5), and  $6.2^\circ$  (NB-6) are found at the end of the simulations. The average kink angles for the segments in the bundle at ca. 200 ps of the simulation are between  $22.5^\circ$  (NB-4),  $6.2^\circ$  (NB-5), and  $7.2^\circ$  (NB-6) (Figure 6). From looking at the kink angles at the end of the simulations there seems to be a trend that an increasing number of segments lower the average kink angle: NB-1,  $25.0^\circ$  (data from ref 15); NB-4,  $20.6^\circ$ ; NB-5,  $13.8^\circ$ ; NB-6,  $8.8^\circ$  (from Figure 6). The dark line in Figure 6 represents the averaged kink angle for each bundle over the time. During the simulation the averaged helix crossing angle remains fairly constant around  $6.5^\circ$ ,  $6.6^\circ$ , and  $3.9^\circ$  (values at 1 ns) for NB-4, NB-5, and NB-6, respectively. There is no translational motion of the bundles along the  $z$ -axis.

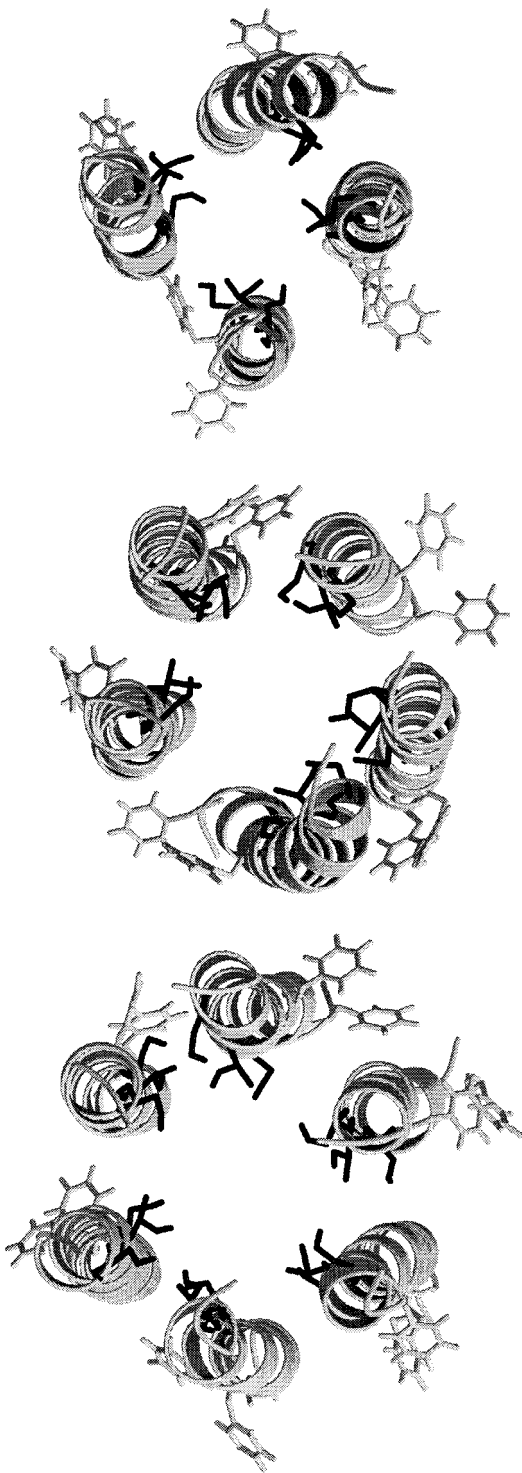


FIGURE 7: View from the N-terminal (top) to the C-terminus (bottom) for NB-4 (top), NB-5 (middle), and NB-6 (bottom). Residues: dark, serines and threonines; light, phenylalanines.

The Phe side chains are still pointing toward the lipid phase at the end of the simulation. The Lys and Arg residues for the NB bundles face the outside of the bundles interacting preferentially with the lipid headgroups rather than with water molecules. Such interactions are also found in natural analogous TM helices (45, 46) and synthetic TM peptides (47). They are seen to anchor the TM region within the polar region of the lipid headgroups. The view from the N-terminal top to the C-terminus gives an impression of the shape of the pore (Figure 7). For the NB bundles the helices remain

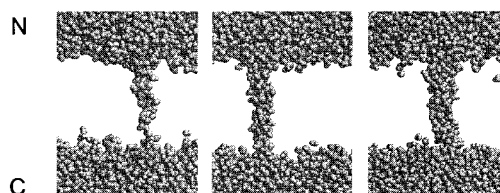


FIGURE 8: Water molecules within each bundle after 1 ns simulation: NB-4 (left), NB-5 (middle), and NB-6 (right).

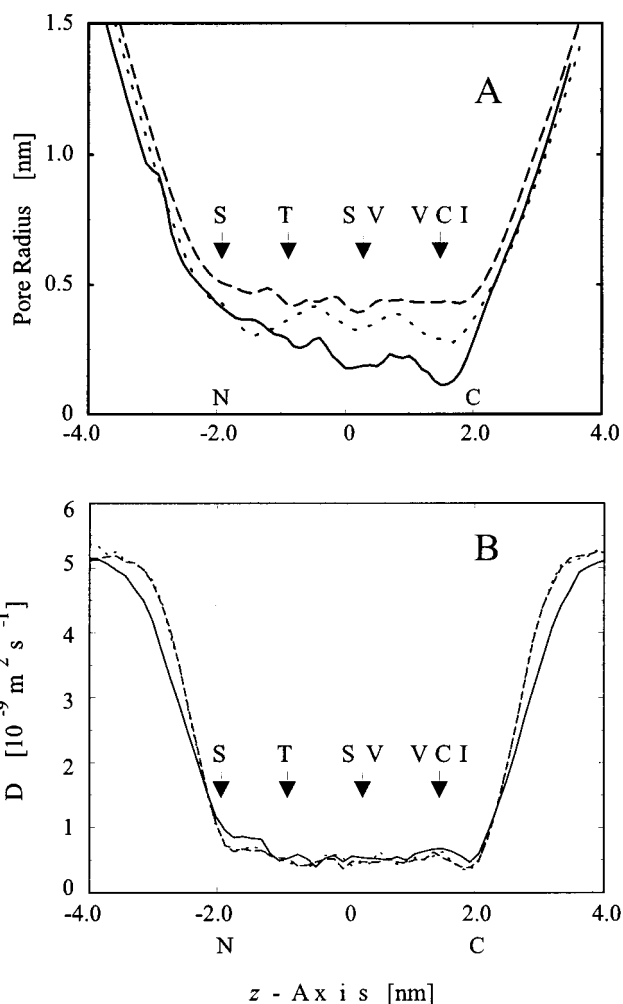


FIGURE 9: (A) Averaged pore radius profile at the end of the simulation [calculated using the program HOLE (14)] (five profiles were averaged, representing the last 250 ps in steps of 50 ps of the simulation). (B) Average diffusion coefficient of water along the pore of the bundles over 1 ns.

at an almost symmetrical position. The robust structure of the bundle leads to an unchanged pore facing positions of the hydrophilic side chains after 1 ns simulation.

*Water in the Pore.* For NB-4 a very narrow column of water molecules is obtained after 1 ns of simulation with ca. 49 water molecules (Figure 8). At its C-terminal end this column is as narrow as one water molecule. When the number of segments is increased, the number of water molecules increase, showing a continuous water column with ca. 105 and ca. 145 waters for NB-5 and NB-6, respectively. The number of waters is the consequence of the pore radius profile (Figure 9A). For NB-4 the radius decreases constantly toward the C-terminal end with a minimum of 1.1 Å around Val-35/Cys-38/Ile-42. Another minimum in the pore radius is found around Ser-28/Val-31. NB-5 does also have its

minimum around Val-35/Cys-38/Ile-42 (ca. 2.8 Å). The minima around Ser-28/Val-31 are less pronounced. For NB-6 the narrowest part is toward the N-terminal end with ca. 3.9 Å around Ser-20. When the number of segments is increased, the overall pore radius increases. For all three channel models the longitudinal diffusion coefficient for the water molecules within the pore drops 10-fold to ca.  $0.5 \times 10^{-9} \text{ m}^2 \text{ s}^{-1}$  for all bundles (Figure 9B). There is no obvious correlation between the diffusivity and the hydrophilic side chains pointing into the pore.

With the pore radius calculated, the conductances for 0.5 M KCl and NaCl solutions are estimated (Table 1) using the program HOLE (14). This program calculates the maximum space within the pore around a point along the *z*-axis. The conductance is the summation of all the conductances for such spheres along the *z*-axis. The values are calculated according to the respective electrolyte solution. The values obtained have to be corrected for the reduced mobility of the ions within the restricted geometry of the pore. Such a correction assumes that the relation between the reduced mobility of the ions within the pore and the reduced mobility of the waters is the same. For water, a decrease of the mobility by a factor of ca. 10 is found, compared to the value for the bulk phase (Figure 9B). The pore formation with four segments from NB leads to an estimated conductance of ca. 22 pS/13 pS for a 0.5 M KCl and NaCl solution, respectively. Bundles of five segments generate conductivity of ca. 56 pS/34 pS (0.5 M KCl/NaCl), and six segments generate conductivity of ca. 88 pS/53 pS. The results for 0.5 M KCl are in agreement with the experimental findings. We assume that all bundles presented here are formed by the transmembrane potential. However, at the moment we cannot decide which of the bundles is the most stable assembly.

## DISCUSSION

**Conductance Measurements.** The level of conductance of the TM segment of NB is in the range of those found for other natural channel-forming purely transmembrane peptides such as  $\delta$ -toxin from *Staphylococcus aureus* (48). This channel-forming peptide exhibits conductances around 70 and 100 pS at low peptide concentration and a conductance of ca. 450 pS at higher peptide concentration in 0.5 M KCl (49). Also, synthetic peptides based on almost the same alternating hydrophilic/hydrophobic residues lining the pore, e.g., H<sub>2</sub>N-(LSSLLSL)<sub>3</sub>-CONH<sub>2</sub> (50), do show ion channel activity with conductance around 70 pS in a 0.5 M KCl solution. Mellitin, an amphiphilic peptide with largely hydrophobic residues lining the pore and some hydrophilic residues at the C-terminal end, shows also conductance of ca. 110 pS in 1.8 M NaCl. In contrast, alamethicin has purely hydrophobic pore-lining residues (51). In a planar lipid bilayer the peptide produces several conductance levels. We obtained currents of ca. 100, 310, 690, and 1180 pS (data not shown) at concentrations of ca. 0.5  $\mu\text{M}$  alamethicin (52, 53). Brief pulses of currents up to ca. 2200 pS are also found. Even if alamethicin usually forms larger assemblies with more than six segments, even small pores (less than six segments) show still quite high conductance levels.

In combination with the pore diameter the hydrophobic walls affect the water structure and, consequently, the

diffusion of the ions through the pore. However, once hydrophilic residues face the pore, the type of hydrophilic amino acid in the pore might not be of too much relevance for generating particular conductance levels.

The current behavior found for NB transmembrane peptide with several conductance states supports the barrel-stave model (54, 55). In this model the channels are formed by a conversion of antiparallel segments to parallel ion-conducting bundles. Integral increase of conductance levels reflects the simultaneous presence of bundles with different numbers of segments (56). Stepwise increase of lower conductance states usually stands for the existence of one or more channels simultaneously open in the bilayer. We find a flickering of the conductance between ca. 50–60 pS and 110–130 pS. Comparison with the computationally derived values suggests bundles consisting of five to six segments. Lower conductance values observed in this study would argue for the occasional existence of bundles with four segments. The width of the data for one conductance level does not completely rule out the existence of multiple channels simultaneously open, each consisting of either five or six segments. As a conclusion of the present data the TM bundles of four, five, and six segments are stable under the conditions reported here.

The natural peptide expressed in *E. coli* and reconstituted in lipid membranes shows mainly conductance of 45 pS (7). In dependence of peptide concentration the level was reported to change between 10 pS and several hundred picosiemens when the protein was incorporated in liposomes at various concentrations prior to fusion with the lipid membrane. This conductance is in agreement with the values found for the TM domain of the peptide in our study. M2 is formed by a pair of covalently linked dimers (57, 58). M2 expressed in *Spodoptera frugiperda* (Sf9) cells and reconstituted in lipid membranes exhibits conductances >25 pS (59). Studies with the synthesized putative TM spanning domain of M2 without any cross-linking reveal minimal conductance of ca. 10 pS (60). Higher conductance levels are interpreted in terms of multiple channels present in the bilayer. For Vpu expressed in *E. coli* and reconstituted in lipid membranes, conductances of 14–280 pS are found (61). The levels are very much depend on the preparation methods. Preparation of liposomes seems to form smaller channel-forming peptide aggregates with lower conductance levels. TM segments of Vpu derived from protein synthesis show distinct channel conductances of 17, 28, 37, and 61 pS in symmetric 0.5 M KCl solution (62). It seems likely that the complete proteins including their extramembraneous parts form stable channels with a slightly higher number of monomers than do the peptides consisting of just their synthetic TM segments.

An increase in channel open times for particular conductance states has been reported for synthetically derived alamethicin dimers compared to their naturally existing monomeric counterparts (63, 64). Since a third conductance level is preliminarily occupied, the data are interpreted in terms of the existence of stable hexamers. We also might see in our study the existence of stable hexameric bundles formed by dimers or bundles of higher even-numbered multiples of the dimers. In principle, we have to take oligomerization of the peptide into account. This oligomerization is a consequence of the condition under which the synthesis and the purification steps were carried out. Thus,

bundles of four, five, and six segments could be readily formed by monomers, as well as dimers and trimers.

Linearity of the current–voltage relation can be observed if the ion does not experience any defined electrostatic gradient within the pore. However, in an assembly of parallel helices the N- and C-termini induce a potential on an ion along the pore. Consequently, all channels based on such an  $\alpha$ -helix assembly should show rectification (65). In a recent study (65) this was shown for uncharged synthetic channel peptides [Ac-(LSSLLSL)<sub>3</sub>]. Rectification is explained by theoretical models defining the experienced potential of an ion within a pore as the summation of (i) a helical dipole potential, (ii) an interfacial polarization potential, and (iii) a constant transmembrane potential. In light of our studies we suggest that the alignment of the water dipoles within the pore might counteract the proposed potential. As a consequence, rectification is at least minimized in the case of the lower conductance levels of the NB peptide.

*Comparison of the Computational Data with Those from Other Channel Peptide Models.* MD simulation of the transmembrane segments of M2 from influenza A in vacuo (66) all show a tilt angle of ca. 15° (starting angle of 6.2°). MD simulations of the M2 tetramer in a lipid bilayer (summarized in ref 67) and based on a mathematical analysis of site-directed mutagenesis data (68) reveal almost identical values. This is slightly higher than for the bundles of NB with similar number of segments. NMR spectroscopic data revealed a tilt angle of ca. 30° for the TM segments of M2 (69). For M2 the helix crossing angle was also higher [21° ± 1° (66), 22° ± 4° (68)] than for the bundles in this study. For Vpu bundles of four, five, and six segments crossing angles of −8.7°, −6.6°, and +10.0°, respectively, have been obtained after 100 ps (70). Also, no supercoiling for Vpu bundles was found (71).

We find that the crossing angles of the helices do not deviate much from the starting value after a 1 ns simulation. This is in common with calculations on other channel-forming peptides, e.g.,  $\delta$ -toxins (72–74) or models of M2 from nicotinic acetylcholine receptor (75). In contrast, simulations on hydrophilic bundles, e.g., Ala-20 do show deviations (76, 77). It seems to be a general feature that bundles of hydrophilic pores remain very close to the initial starting values during the simulations.

The comparison reveals that the NB bundle behaves like a typical “hydrophilic” ion channel in terms of its topology.

*Water in the Pores.* Simulations of the behavior of water in a narrow column showed that the rotational reorientation rate is lowered compared to bulk water. Similar results were obtained for hydrophilic (Alm) and hydrophobic bundles (M2 from nicotinic acetylcholine receptor) (78) and explained by the pore radius and the presence of the hydrophilic side chains in the pore. Immobilization of the water molecules is expected to alter the local dielectric constant of water within pores (79). As a consequence, the diffusion coefficient of cations and anions is lowered compared to their bulk values (80). The independence of the orientation of the water molecules from the pore radius (data not shown) indicates that the water orientation is due to the peptide backbone. A detailed analysis of the fraction of hydrogen bonding (15, 22) of the side chains Ser, Thr, Arg, and Lys (data not shown) revealed that all side chains form stable H-bonds with either

the backbone or neighboring side chains within the same segment. In some cases H-bonds with adjacent segments are also found. All bundles in common are H-bonding of the hydrophilic side chains with pore water molecules which can be best described by a high number of hydrogen-bonding partners combined with a short time period during which they actually form hydrogen bonds. This means that the hydrophilic side chains Ser and Thr fit “perfectly” into the pore water network in such a way that they do not affect the orientation of the water molecules.

For the water molecules we use the SPC model (81). The insensitivity of the water parameters on the actual pore-facing residues might be a result of the limitation of the water model used in this study. Thus, at the moment we cannot give any clear answer on how the hydrophilic side chain motives in NB (S<sup>20</sup>T<sup>24</sup>S<sup>28</sup>) affect the ion permeation on a structural level.

## CONCLUSIONS

NB transmembrane channel peptide has been modeled as a predominantly  $\alpha$ -helical structure in methanol and in lipid membranes. The peptide assembles to form ion channels with several conductance levels following a linear I–V relationship. The conductance of the whole peptide is determined by the formation of the transmembrane segments. Simulations on the peptide bundles in a fully hydrated lipid bilayer result in similar conductance levels as found experimentally. From this observation we conclude that bundles of four to six segments might be responsible for the experimental results.

## ACKNOWLEDGMENT

Thanks are due to Dr. I. Shrivastava and Dr. P. Tieleman for valuable discussions. We thank Dr. R. T. Aplin (Oxford) for performing the mass spectroscopy and Dr. A. Willis (Oxford) for doing the peptide sequence analysis. The use of the computer facilities of the Oxford Supercomputing Centre is acknowledged.

## REFERENCES

1. Shaw, M. W., Choppin, P. W., and Lamb, R. A. (1983) *Proc. Natl. Acad. Sci. U.S.A.* 80, 4879–4883.
2. Williams, M. A., and Lamb, R. A. (1986) *Mol. Cell. Biol.* 6, 4317–4328.
3. Shaw, M. W., and Choppin, P. W. (1984) *Virology* 139, 178–184.
4. Betakova, T., Nermut, M., and Hay, A. (1996) *J. Gen. Virol.* 77, 2689–2694.
5. Brassard, D. L., Leser, G. P., and Lamb, R. A. (1996) *Virology* 220, 350–360.
6. Lamb, R. A., and Pinto, L. H. (1997) *Virology* 229, 1–24.
7. Sunstrom, N. A., Prekumar, L. S., Prekumar, A., Ewart, G., Cox, G. B., and Gage, P. W. (1996) *J. Membr. Biol.* 150, 127–132.
8. Chizhnikov, I., Ogden, D., Betakova, T., Phillips, A., and Hay, A. (1998) *Biophys. J.* 74, A319.
9. Holsinger, L. J., Nichani, D., Pinto, L. H., and Lamb, R. A. (1994) *J. Virol.* 68, 1551–1563.
10. Pinto, L. H., Tu, Q., Sakeguchi, T., Gandhi, C., and Lamb, R. A. (1997) *Biophys. J.* 72, A109.
11. Mould, J. A., Li, H.-C., Dudlak, C. S., Lear, J. D., Pekosz, A., Lamb, R. A., and Pinto, L. H. (2000) *J. Biol. Chem.* 275, 8592–8599.
12. Sansom, M. S. P., Forrest, L. R., and Bull, R. (1998) *BioEssays* 20, 992–1000.

13. Smart, O. S., Goodfellow, J. M., and Wallace, B. A. (1993) *Biophys. J.* 65, 2455–2460.
14. Smart, O. S., Breed, J., Smith, G. R., and Sansom, M. S. P. (1997) *Biophys. J.* 72, 1109–1126.
15. Fischer, W. B., Forrest, L. R., Smith, G. R., and Sansom, M. S. P. (2000) *Biopolymers* 53, 529–538.
16. Mao, D., Wachter, E., and Wallace, B. A. (1982) *Biochemistry* 21, 4960–4968.
17. Chang, C. T., Wu, C.-S. C., and Yang, J. T. (1978) *Anal. Biochem.* 91, 13–31.
18. Montal, M., and Mueller, P. (1972) *Proc. Natl. Acad. Sci. U.S.A.* 69, 3561–3566.
19. Kerr, I. D., Sankaramakrishnan, R., Smart, O. S., and Sansom, M. S. P. (1994) *Biophys. J.* 67, 1501–1515.
20. Brünger, A. T. (1992) *X-PLOR Version 3.1. A System for X-ray Crystallography and NMR*, Yale University Press, New Haven, CT.
21. Brooks, B. R., Bruccoleri, R. E., Olafson, B. D., States, D. J., Swaminathan, S., and Karplus, M. (1983) *J. Comput. Chem.* 4, 187–217.
22. Forrest, L. R., Tieleman, D. P., and Sansom, M. S. P. (1999) *Biophys. J.* 76, 1886–1896.
23. Tieleman, D. P., Sansom, M. S. P., and Berendsen, H. J. C. (1999) *Biophys. J.* 76, 40–49.
24. Kabsch, W., and Sander, C. (1983) *Biopolymers* 22, 2577–2637.
25. Wallace, B. A., and Mao, D. (1984) *Anal. Biochem.* 142, 317–328.
26. Chen, Y., and Wallace, B. A. (1997) *Biophys. Chem.* 65, 65–74.
27. Cascio, M., and Wallace, B. A. (1995) *Anal. Biochem.* 227, 90–100.
28. Wallace, B. A., and Corder, R. (1997) *J. Pept. Res.* 49, 331–335.
29. Tatulian, S. A., and Tamm, L. K. (2000) *Biochemistry* 39, 496–507.
30. Dubovski, P., Li, H.-C., Takahashi, S., Arseniev, A. S., and Akasaka, K. (2000) *Protein Sci.* 9, 786–798.
31. Manavalan, P., and Johnson, W. C. (1987) *Anal. Biochem.* 167, 76–85.
32. Provencher, S. W., and Glockner, J. (1981) *Biochemistry* 20, 33–37.
33. Sreerema, N., Venyaminov, S. Y., and Woody, R. W. (1999) *Protein Sci.* 8, 370–380.
34. Kerr, I. D., Dufourcq, J., Rice, J. A., Fredkin, D. R., and Sansom, M. S. P. (1995) *Biochim. Biophys. Acta* 1236, 219–227.
35. Zhong, Q., Husslein, T., Moore, P. B., Newns, D. M., Pattnaik, P., and Klein, M. L. (1998) *FEBS Lett.* 434, 265–271.
36. Sankaramakrishnan, R., Adcock, C., and Sansom, M. S. P. (1996) *Biophys. J.* 71, 1659–1671.
37. Ortells, M. O., Barrantes, G. E., Wood, C., Lunt, G. G., and Barrantes, F. J. (1997) *Protein Eng.* 10, 511–517.
38. Zhong, Q., Jiang, Q., Moore, P. B., Newns, D. M., and Klein, M. L. (1998) *Biophys. J.* 74, 3–10.
39. Changeux, J. P., Galzi, J. I., Devillers-Thiéry, A., and Bertrand, D. (1992) *Q. Rev. Biophys.* 25, 395–432.
40. Lester, H. (1992) *Annu. Rev. Biophys. Biomol. Struct.* 21, 267–292.
41. Hucho, F., Tsetlin, V., and Machold, J. (1996) *Eur. J. Biochem.* 239, 539–557.
42. Hirsch, A., Wacker, T., Weckesser, J., Diederichs, K., and Wolfram, W. (1995) *Proteins: Struct., Funct., Genet.* 23, 282–284.
43. Forrest, L. R., Kukol, A., Arkin, I. T., Tieleman, D. P., and Sansom, M. S. P. (2000) *Biophys. J.* 78, 55–69.
44. Branden, C., and Tooze, J. (1991) *Introduction to Protein Structure*, Garland, New York.
45. Shrivastava, I. H., Capener, C. E., Forrest, L. R., and Sansom, M. S. P. (2000) *Biophys. J.* 78, 79–92.
46. Monne, M., Nilsson, I., Johansson, M., Elmhed, N., and von Heijne, G. (1998) *J. Mol. Biol.* 284, 1177–1183.
47. Belohorcova, K., Davis, J. H., Woolf, T. B., and Roux, B. (1997) *Biophys. J.* 73, 3039–3055.
48. Fitton, J. E., Dell, A., and Shaw, W. V. (1980) *FEBS Lett.* 115, 209–212.
49. Mellor, I. R., Thomas, D. H., and Sansom, M. S. P. (1988) *Biochim. Biophys. Acta* 942, 280–294.
50. Lear, J. D., Wasserman, Z. R., and DeGrado, W. F. (1988) *Science* 240, 1177–1181.
51. Woolley, G. A., and Wallace, B. A. (1992) *J. Membr. Biol.* 129, 109–136.
52. Hanke, W., and Boheim, G. (1980) *Biochim. Biophys. Acta* 596, 456–462.
53. Sansom, M. S. P. (1991) *Prog. Biophys. Mol. Biol.* 55, 139–236.
54. Boheim, G. (1974) *J. Membr. Biol.* 19, 277–303.
55. Baumann, G., and Mueller, P. (1974) *J. Supramol. Struct.* 2, 538–557.
56. Sansom, M. S. P., Kerr, I. D., and Mellor, I. R. (1991) *Eur. Biophys. J.* 20, 229–240.
57. Sugrue, R. J., and Hay, A. J. (1991) *Virology* 180, 617–624.
58. Sakaguchi, T., Tu, Q. A., Pinto, L. H., and Lamb, R. A. (1997) *Proc. Natl. Acad. Sci. U.S.A.* 94, 5000–5005.
59. Tosteson, M. T., Pinto, L. H., Holsinger, L. J., and Lamb, R. A. (1994) *J. Membr. Biol.* 142, 117–126.
60. Duff, K. C., and Ashley, R. H. (1992) *Virology* 190, 485–489.
61. Ewart, G. D., Sutherland, T., Gage, P. W., and Cox, G. B. (1996) *J. Virol.* 70, 7108–7115.
62. Schubert, U., Ferrier-Montiel, A. V., Oblatt-Montal, M., Henklein, P., Streb, K., and Montal, M. (1996) *FEBS Lett.* 398, 12–18.
63. You, S., Peng, S., Lien, L., Breed, J., Sansom, M. S. P., and Woolley, G. A. (1996) *Biochemistry* 35, 6225–6232.
64. Jaikaran, D. C. J., Biggin, P. C., Wenschuh, H., Sansom, M. S. P., and Woolley, G. A. (1997) *Biochemistry* 36, 13873–13881.
65. Kienker, P. K., DeGrado, W. F., and Lear, J. D. (1994) *Proc. Natl. Acad. Sci. U.S.A.* 91, 4859–4863.
66. Sansom, M. S. P., Kerr, I. D., R., S. G., and Son, H. S. (1997) *Virology* 233, 163–173.
67. Forrest, L. R., DeGrado, W. F., Dieckmann, G. R., and Sansom, M. S. P. (1998) *Folding Des.* 3, 443–448.
68. Pinto, L. H., and DeGrado, W. F. (1997) *Proc. Natl. Acad. Sci. U.S.A.* 94, 11301–11306.
69. Kovacs, F. A., and Cross, T. A. (1997) *Biophys. J.* 73, 2511–2517.
70. Grice, A., Kerr, I. D., and Sansom, M. S. P. (1997) *FEBS Lett.* 405, 299–304.
71. Moore, P. B., Zhong, Q., Husslein, T., and Klein, M. L. (1998) *FEBS Lett.* 431, 143–148.
72. Mellor, I. R., Thomas, D. H., and Sansom, M. S. P. (1988) *Biochim. Biophys. Acta* 942, 280–294.
73. Kerr, I. D., Doak, D. G., Sankaramakrishnan, R., Breed, J., and Sansom, M. S. P. (1996) *Protein Eng.* 9, 161–171.
74. Gazit, E., Bach, D., Kerr, I. D., Sansom, M. S. P., Chejanovsky, N., and Shai, Y. (1994) *Biochem. J.* 304, 895–902.
75. Sankaramakrishnan, R., and Sansom, M. S. P. (1995) *FEBS Lett.* 377, 377–382.
76. Breed, J., Sankaramakrishnan, R., Kerr, I. D., and Sansom, M. S. P. (1995) *Biophys. J.* 70.
77. Oliver, A. E., and Deamer, D. W. (1994) *Biophys. J.* 66, 1364–1379.
78. Breed, J., Sankaramakrishnan, R., Kerr, I. D., and Sansom, M. S. P. (1996) *Biophys. J.* 70, 1643–1661.
79. Sansom, M. S. P., Kerr, I. D., Breed, J., and Sankaramakrishnan, R. (1996) *Biophys. J.* 70, 693–702.
80. Smith, G. R., and Sansom, M. S. P. (1999) *Biophys. Chem.* 79, 129–151.
81. Hermans, J., Berendsen, H. J. C., van Gunsteren, W. F., and Postma, J. P. M. (1984) *Biopolymers* 23, 1513–1518.